Acta Materia Medica

Research Article

ZnPc photosensitizer-loaded peony-shaped $FeSe_2$ remotely controlled by near-infrared light for antimycobacterial therapy

Graphical abstract

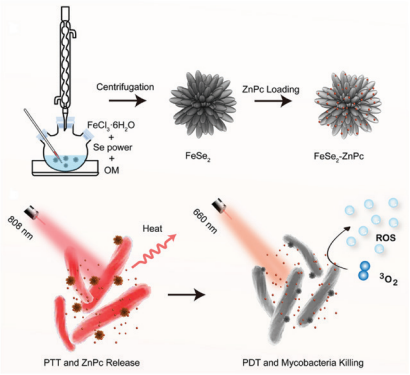

Highlights

- A smart PDT system is developed to combine peony-shaped ferroselite $FeSe_2$ with zinc (II) phthalocyanine (ZnPc) photosensitizers.
- The photothermal effect of $FeSe_2$ prompted the release of ZnPc from $FeSe_2$-ZnPc.
- $FeSe_2$-ZnPc achieve a robust photodynamic/photothermal antibacterial capability.

Authors

Peng Wu, Xiaoning Liu, Yuheng Duan, Liping Pan, Zhaogang Sun, Hongqian Chu, Chuanzhi Zhu and Bei Liu

Correspondence

chuhongqian@bjxkyy.cn (H. Chu); chuanzhizhu@gmail.com (C. Zhu); liubei@muc.edu.cn (B. Liu)

In brief

A smart system based on peony-shaped $FeSe_2$ and zinc (II) phthalocyanine (ZnPc) PSs with activatable photodynamic and robust photothermal antibacterial capability was developed.

https://doi.org/10.15212/AMM-2023-0012

Acta Materia Medica

Research Article

ZnPc photosensitizer-loaded peony-shaped $FeSe_2$ remotely controlled by near-infrared light for antimycobacterial therapy

Peng Wu[a,1], Xiaoning Liu[a,1], Yuheng Duan[b], Liping Pan[b], Zhaogang Sun[b], Hongqian Chu[b,*], Chuanzhi Zhu[b,*] and Bei Liu[a,*]

[a]College of Science, Minzu University of China, Beijing, 100081, China
[b]Beijing Key Laboratory for Drug Resistance Tuberculosis Research, Beijing Tuberculosis and Thoracic Tumor Research Institute, Beijing Chest Hospital, Capital Medical University, Beijing, 101149, China

[1]These authors contributed equally to this work.
***Correspondence:** chuhongqian@bjxkyy.cn (H. Chu); chuanzhizhu@gmail.com (C. Zhu); liubei@muc.edu.cn (B. Liu)

Received: 11 April 2023; Revised: 15 June 2023; Accepted: 19 June 2023

Published online: 27 June 2023

DOI 10.15212/AMM-2023-0012

ABSTRACT

The development of novel antimicrobial agents is highly desirable for treating bacterial infections. Here, a smart photodynamic therapy (PDT) system based on a combination of peony-shaped ferroselite $FeSe_2$ particles and zinc (II) phthalocyanine (ZnPc) photosensitizers was constructed. Effective energy transfer occurred from ZnPc to $FeSe_2$, because of their proximity, thus eliciting the OFF state of ZnPc photosensitizers. Under 808 nm NIR light irradiation, the photothermal effect of $FeSe_2$ promoted the release of ZnPc, thus turning on the photodynamic effect of the photosensitizers (ON state). In vitro, $FeSe_2$-ZnPc exhibited high photo-to-thermal conversion efficiency (26.4%) and effective generation of reactive oxygen species for combined photothermal/photodynamic therapy. Therefore, the $FeSe_2$-ZnPc hybrids have great potential to serve as alternatives to antibiotics for eradication of pathogenic bacteria.

Keywords: peony-shaped $FeSe_2$, NIR activatable, photothermal therapy, photodynamic therapy

1. INTRODUCTION

Mycobacteria, particularly tuberculosis-causing *Mycobacterium tuberculosis* (*M. tb*), pose a serious threat to global health [1-4]. The current first-line treatment heavily relies on antibiotics, thereby resulting in the emergence of multidrug-resistant *M. tb* and high mortality in humans [5-8]. Therefore, an urgent need exists for the rational development of antimicrobial agents with novel mechanisms of action. In the past decade, antibacterial nanomaterials have become contenders as antibacterial treatments for use when traditional antibiotics fail. This emerging area of antibiotics includes many nanostructured materials, including nanocarriers loaded with antibiotics [9], noble metals or metal oxide nanoparticles [9-12], graphene or graphene oxide [13-15], organic–inorganic nanocomposites [16, 17], carbon nanotubes/dendrimers [18], self-assembled or unimolecular micelles [19, 20], and supramolecular nanoparticles [21, 22]. Although different types of antibacterial nanomaterials show substantial differences in their antimicrobial behavior, they share antimicrobial advantages such as minimal invasiveness, broad-spectrum antibacterial properties, and low drug resistance.

Specifically, drug-free nanosystems based on photodynamic therapy (PDT) are considered an emerging noninvasive modality for antibacterial treatment [23-27]. PDT uses photosensitizers (PSs) that absorb light and transfer tissue oxygen to reactive oxygen species (ROS) to kill bacteria. However, the short lifetime (<0.04 μs) and small active regions (<0.02 μm) of ROS are formidable challenges in PDT. In addition, the "always-active" model and the low selectivity of the currently used PSs can induce unexpected phototoxicity in both tumor and normal tissues, thus potentially damaging normal tissues and causing long-lasting cutaneous photosensitivity [28, 29]. To overcome these limitations, "smart" PSs have been developed to provide an additional level of control (beyond light and PS presence) of ROS generation. These smart PSs are designed to be quenched ("OFF" state) before administration. After accumulating in target tumor tissues, PSs are turned on (dequenched)

via predetermined stimuli, such as protein, pH, DNA, or thiol responses [29, 30-34]. Among these stimuli, near-infrared (NIR) light lasers have attracted great interest because of their noninvasiveness and deep tissue penetration. NIR-sensitive nanocarriers, such as Au nanorods and graphene oxide, have been developed to turn off PSs [35, 36]. After NIR laser irradiation, the PS is released from NIR-sensitive nanocarriers and becomes highly phototoxic. Despite research progress, the strategy often has drawbacks of complicated molecular design, time-consuming synthesis, and relatively low antibacterial efficacy. The development of a simple approach for highly efficient activatable PDT is urgently needed.

Here, we present the design of a smart PS for photothermal-activatable PDT. The platform was constructed by functionalization of a peony-shaped $FeSe_2$ with typical zinc (II) phthalocyanine (ZnPc) PSs (**Scheme 1a**). Effective energy transfer occurs between ZnPc PSs and $FeSe_2$ because of their proximity, thus resulting in a nonphototoxic state of PSs (OFF state). Under NIR irradiation, the photothermal effect of $FeSe_2$ promotes the release of PSs from the $FeSe_2$ surface, thus turning on the photodynamic effect of PSs (ON state). Notably, $FeSe_2$ not only acts as a smart carrier of PSs but also provides a highly efficient photothermal therapy (PTT) effect for enhanced antibacterial therapy. This activatable platform has robust photodynamic/photothermal antibacterial capability and therefore has great potential for broad-spectrum eradication of mycobacteria (**Scheme 1b**).

2. MATERIALS AND METHODS

2.1 Reagents

$FeCl_3 \cdot 6H_2O$ was purchased from Aldrich. Se powder was purchased from Alfa Aesar. Oleylamine was purchased from Acros Organics Chemicals. Zinc phthalocyanine (ZnPc) and Tween 80 were purchased from Sigma-Aldrich. Tetrahydrofuran (THF) was obtained from J&K Scientific Ltd (San Jose, CA, USA). Singlet oxygen sensor green (SOSG) was obtained from Meilunbio. Difco™ Middlebrook 7H9 medium, 7H10 medium, and oleic acid–albumin–dextrose–catalase (OADC) were purchased from BD Biosciences (Rutherford, NJ,

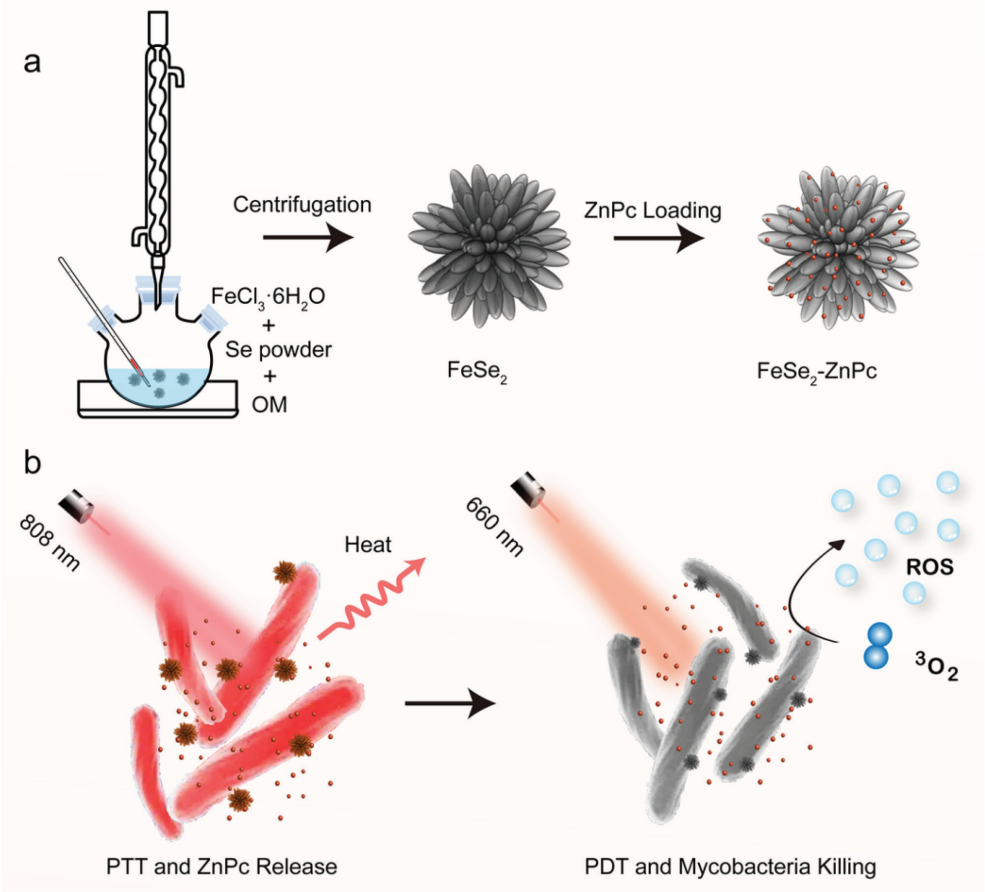

Scheme 1 | Schematic illustration of (a) the synthesis of $FeSe_2$-ZnPc and (b) its application in mycobacterial therapy through a combination of PTT and PDT.

Acta Materia Medica

US). Glycerol was obtained from Sinopharm Chemical Reagent Co., Ltd (Shanghai, China). Deionized water (Millipore Milli-Q grade) with a resistivity of 18.2 MU was used in the experiments. All chemicals were used as received without further purification.

2.2 Synthesis of $FeSe_2$-ZnPc

$FeCl_3 \cdot 6H_2O$ (1.0 mmol) and Se powder (2.0 mmol) were mixed with 10 mL of oleylamine in a 100 mL three-neck flask. Under mild stirring, the reaction mixture was heated to 120°C for 1 h under a nitrogen atmosphere. Subsequently, the temperature was increased to 180°C for another 1 h. The flask was then allowed to cool to room temperature. The $FeSe_2$ product (black precipitate) was harvested via centrifugation and then washed three times with THF. For generation of $FeSe_2$-ZnPc, 1 mL of ZnPc was added to 1 mL of $FeSe_2$ solution. The mixture was stirred at room temperature for 24 h. The resulting $FeSe_2$-ZnPc products were collected by centrifugation, washed with THF and ethanol several times, and dispersed in deionized water at 4°C for further use.

2.3 Characterizations

The size and morphology of the products were recorded with scanning electron microscopy (SEM) (Hitachi SU8220) and high revolution transmission electron microscopy (TEM) (JEM-1200EX). The ζ-potentials were determined by electrophoretic mobility measurement (Zetasizer Nano ZS). The absorption spectra were measured with a UV–vis spectrometer (V-750, JASCO). The fluorescence emission spectra were measured with a F-4500 fluorescence spectrometer (F-4500, Hitachi). X-ray diffraction (XRD) was performed on a D/MAX-TTRIII (CBO) series XRD instrument at 40 kV and 200 mA. Infrared-radiation thermal images were monitored through an infrared-radiation thermal camera (TiS65, Fluke).

2.4 NIR-laser-induced photothermal conversion

The temperature curves of $FeSe_2$-ZnPc solutions were recorded under 808 nm NIR laser irradiation. Briefly, different concentrations of $FeSe_2$-ZnPc solutions (0.25, 0.5, and 1.0 mg/mL) were prepared and irradiated by an 808 nm NIR laser (BWT Beijing Ltd, Beijing, China) with a power density of 1.0 W/cm^2. The temperatures of the $FeSe_2$-ZnPc solutions were monitored every 30 s with a thermal imaging camera. When the solution reached a steady-state temperature (6 min), the laser was shut off. The temperature of distilled water was used as a control.

The photothermal conversion efficiency (η) of $FeSe_2$-ZnPc was calculated as follows: $FeSe_2$-ZnPc solution was irradiated by an 808 nm NIR laser (1.0 W/cm^2) for 6 min. Subsequently, the laser was shut off. The temperatures during the heating and cooling process were recorded. The time constant was determined by application of linear time data versus ln θ from the cooling stage of the $FeSe_2$-ZnPc solution.

2.5 ZnPc release from $FeSe_2$-ZnPc

NIR light-triggered release of ZnPc was investigated. The $FeSe_2$-ZnPc solution was kept in the dark or irradiated by an 808 nm NIR laser (1.0 W/cm^2). Subsequently, the solutions were submitted to centrifugation at several time points (0, 1, 2, 3, 4, or 5 min). The supernatant containing free ZnPc was collected for quantitative analysis with a UV–vis spectrophotometer.

2.6 NIR-activatable ROS generation of $FeSe_2$-ZnPc

The ROS generation of $FeSe_2$-ZnPc was detected with SOSG as an indicator in an aqueous environment. Typically, 1 mL of $FeSe_2$-ZnPc solution was incubated with 5 μL SOSG stock solution (5 mM). The mixture was irradiated by an 808 nm light laser (1.0 W/cm^2) and/or 640 nm light laser (0.1 W/cm^2). The fluorescence emission of SOSG was recorded by a fluorescence spectrophotometer with an excitation wavelength of 488 nm.

2.7 Antibacterial activity testing

The *M. smegmatis* mc^2–155 strain (*M. smeg*) was from our laboratory. The strains were cultured in 7H9 medium supplemented with 10% OADC, 0.05% (v/v) Tween 80 detergent for protein solubilization, and 0.2% (v/v) glycerol at 37°C. *M. smeg* was incubated in 7H9 medium with PBS (1:100, V/V) as a negative control, or $FeSe_2$-ZnPc was added at a final concentration 25 μg/ml for 6 h, and photoirradiation was performed with an 808 nm laser (1.0 W/cm^2) and/or 640 nm laser (0.1 W/cm^2) (with a 10 min break after 2 min irradiation). For the $FeSe_2$-ZnPc-808–640 group, the strain suspension was subjected to 808 nm laser irradiation for 20 min followed by 640 nm light for 20 min. After another 24 h of incubation, the strains were serially diluted 10-fold. Finally, the selected dilutions were plated on 7H10 medium supplemented with 10% OADC and 0.2% (v/v) glycerol at 37°C for 3 days. The colony forming units (CFU) were subsequently enumerated. *Escherichia coli* (*E. coli*) DH5α was purchased from TransGen Biotech. Ltd. Luria Bertani (LB) medium with or without bacterial agar was used for the liquid culture steps and CFU counts. The bacteria were cultured in LB broth and incubated overnight in a shaker at 220 rpm/min at 37°C. On the second day, the bacteria were inoculated in fresh LB broth at a 1:50 (V/V) dilution. Subsequently, $FeSe_2$-ZnPc (10 μg/mL), or an equal volume of LB as a control, was added. Cultures were incubated for 2 h in a shaker 220 rpm/min at 37°C. After exposure to light and another 4 h of incubation, the bacteria were serially diluted 10-fold and plated on LB solid medium. The subsequent treatment and irradiation steps were as described for *M. smeg*.

2.8 Data analysis

Analysis of the data was performed in IBM SPSS ver. 15 (IBM Inc., Armonk, NY). One-way analysis of variance followed by Tukey's test was used to compare more than two groups. A p value <0.05 was considered significant.

3. RESULTS AND DISCUSSION

3.1 Successful synthesis and characterization of $FeSe_2$-ZnPc

$FeSe_2$-ZnPc was synthesized according to the process depicted in Scheme 1. First, $FeSe_2$ was prepared through a simple solution-phase method. SEM and TEM images indicated that the as-prepared $FeSe_2$ had a uniform size (1.48 μm) and peony-shaped morphology (Figure 1a-c, Figure S1). The XRD pattern showed sharp peaks corresponding to the orthorhombic structure of $FeSe_2$, thereby confirming the high crystallinity of the as-synthesized $FeSe_2$ (Figure 1d). The UV–vis–NIR absorption spectrum of $FeSe_2$ showed broad absorption from the UV to the NIR-II range (Figure 1e), in agreement with the black color of the $FeSe_2$ solution. Subsequently, the ZnPc molecules were loaded on the $FeSe_2$ surface. The loading content of ZnPc was determined to be 3.2%. The absorption spectrum of $FeSe_2$-ZnPc exhibited characteristic peaks of ZnPc (Figure 1e). In addition, zeta potential measurement indicated that $FeSe_2$ was positively charged (7.5 mV) and became negatively charged (–12.5 mV) after surface modification with ZnPc (Figure 1f). In addition, the FTIR spectra of $FeSe_2$ and $FeSe_2$-ZnPc confirmed the successful attachment of ZnPc on $FeSe_2$ (Figure S2).

3.2 Photothermal performance of $FeSe_2$-ZnPc

The strong NIR absorption of $FeSe_2$ motivated us to study its NIR-triggered photothermal properties. NIR light (808 nm light) was chosen for excitation, because of its minimal heating effects and high tissue penetrability [37, 38]. As shown in Figure 2a, $FeSe_2$-ZnPc had good photothermal properties under 808 nm NIR light irradiation. The temperature of the $FeSe_2$-ZnPc dispersions increased to 69.5°C in 6 min, whereas the temperature of pure water increased to only 27.2°C. In addition, the temperature of $FeSe_2$-ZnPc increased in a manner dependent on concentration and irradiation duration (Figure 2b), thus demonstrating the highly efficient photothothermal conversion ability of $FeSe_2$-ZnPc. The photothermal conversion efficiency (η) of $FeSe_2$-ZnPc was calculated to be 26.4% (Figure 2c). Furthermore, the photothermal effects were sustained during four ON/OFF cycles of 808 nm NIR light irradiation (an 808 nm light laser at 1.0 W/cm^2, with 6 min laser irradiation for

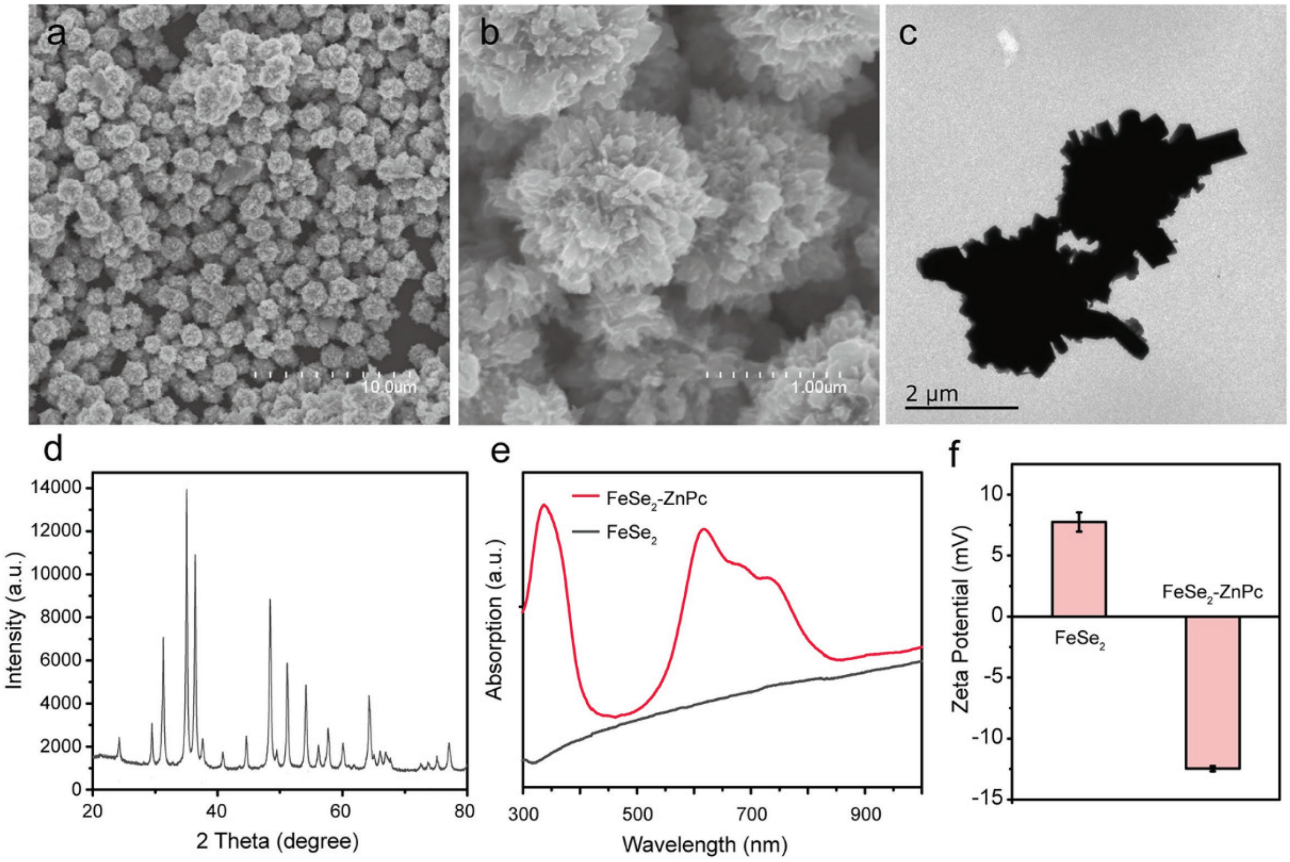

Figure 1 | Characterization of $FeSe_2$-ZnPc.
(a, b) SEM images, (c) TEM image, and (d) XRD pattern of $FeSe_2$. (e) Absorption spectra and (f) zeta potentials of $FeSe_2$ and $FeSe_2$-ZnPc.

Acta
Materia
Medica

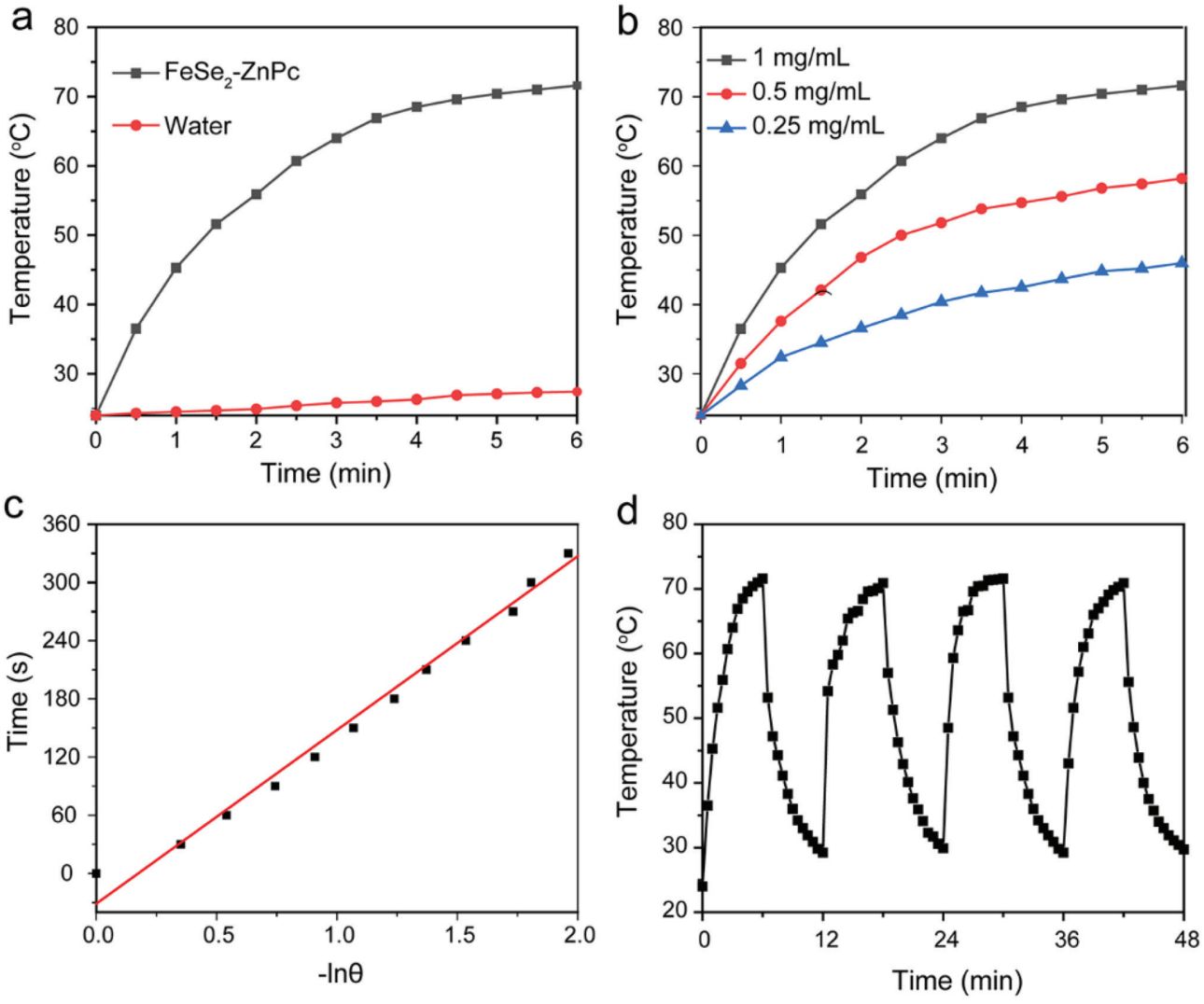

Figure 2 | Photothermal performance of $FeSe_2$-ZnPc.
(a) Temperature variation curves of water and $FeSe_2$-ZnPc solution under 808 nm laser irradiation. (b) Temperature variation curves of different concentrations of $FeSe_2$-ZnPc solutions under 808 nm laser irradiation. (c) Plot of cooling time versus the negative natural logarithm of the temperature driving force. The calculated time constant is τ_s = 204.5 s. (d) Temperature changes in the $FeSe_2$-ZnPc solution over four ON/OFF irradiation cycles.

each cycle) without apparent changes in the peak temperature and the time to reach a plateau (Figure 2d). The effective photothermal performance and excellent photostability of $FeSe_2$-ZnPc make it a favorable agent for PTT.

3.3 NIR-activatable PDT

To test the 808 nm NIR light-triggered release of ZnPc from $FeSe_2$-ZnPc, we first prepared a standard curve, given the linear relationship between ZnPc concentration and absorption intensity (Figure 3a). Subsequently, the release profiles of ZnPc were monitored. Briefly, the $FeSe_2$-ZnPc solution was kept in the dark or irradiated by an 808 nm NIR laser (1.0 W/cm^2) for 1, 2, 3, 4, or 5 min. The supernatants were collected from the suspension by centrifugation, and the amount of ZnPc released was quantified with UV–vis spectroscopy. After 808 nm NIR laser irradiation, a rapid burst release (60%) of the loaded ZnPc was observed in the first 1 min, and 75.3% of ZnPc was released from $FeSe_2$-ZnPc within 5 min (Figure 3b). In contrast, less than 18% of ZnPc was released without NIR irradiation. We speculated that the rapid heat generation of $FeSe_2$ weakened the interaction between ZnPc and $FeSe_2$, thus leading to higher release efficiency of ZnPc. Furthermore, the pH release profiles of ZnPc from $FeSe_2$-ZnPc did not differ between pH 5.5 and 7.4 (Figure S3), thus confirming that pH had no effect on ZnPc release.

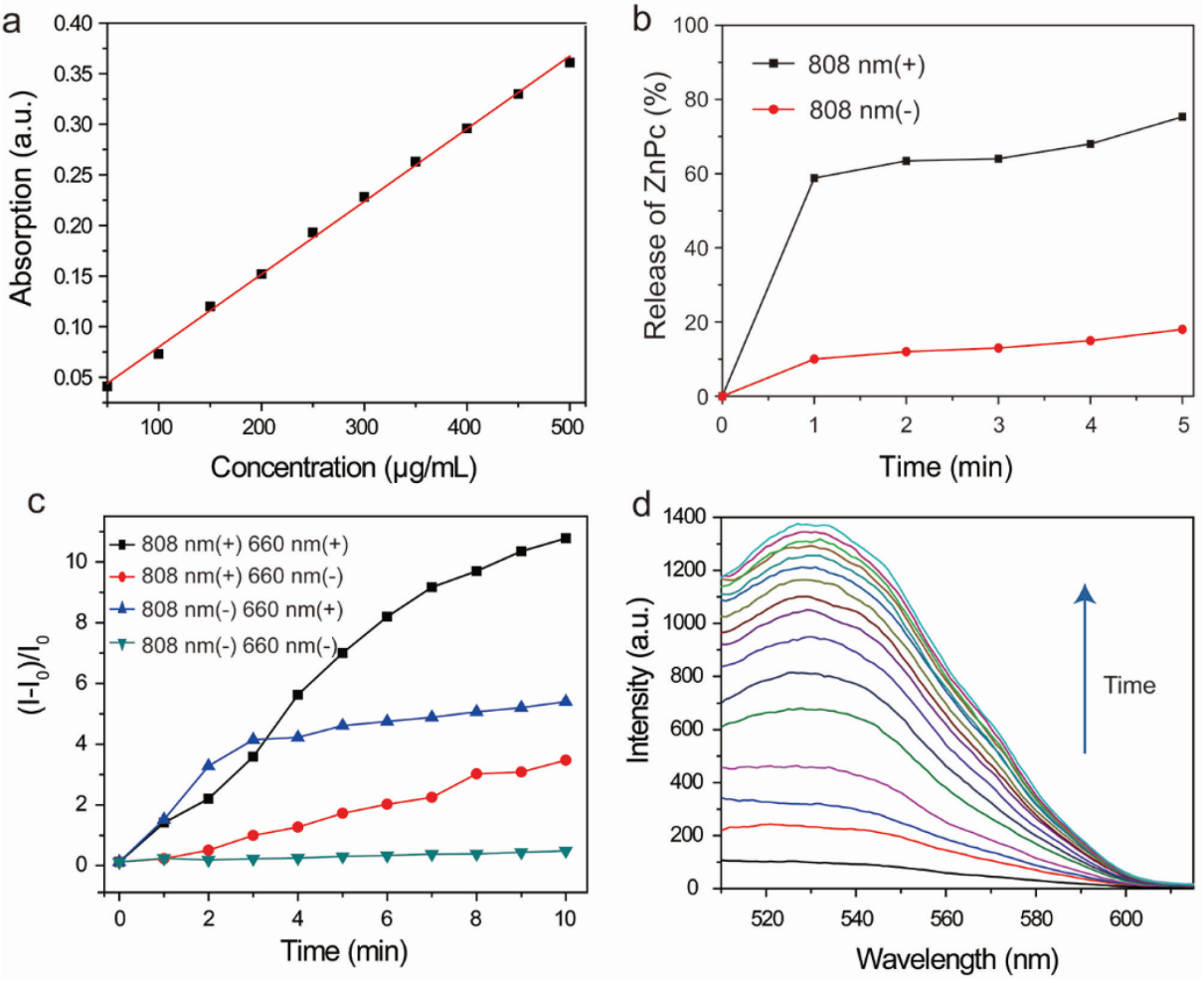

Figure 3 | ZnPc release behavior and singlet oxygen generation of $FeSe_2$-ZnPc.
(a) Linear relationship between the concentrations of ZnPc and their corresponding absorption intensity. (b) ZnPc release curves of $FeSe_2$-ZnPc in PBS with or without 808 nm NIR irradiation. (c) Singlet oxygen generation by $FeSe_2$-ZnPc with or without 808/640 nm light irradiation, detected with SOSG assays. (d) Fluorescence spectra of SOSG solution incubated with $FeSe_2$-ZnPc after 808 nm and 640 nm light irradiation for different times.

This high release efficiency of ZnPc under 808 nm NIR irradiation encouraged us to test the controlled ROS generation of $FeSe_2$-ZnPc. SOSG, whose fluorescence increases after oxidation by ROS, was chosen as an ROS indicator to assess the ROS generation ability of $FeSe_2$-ZnPc. The fluorescence intensity of SOSG in the $FeSe_2$-ZnPc solution increased under 640 nm light irradiation (Figure 3c, d). In contrast, the $FeSe_2$-ZnPc solution without light irradiation did not generate ROS, thus indicating the photodynamic effect of $FeSe_2$-ZnPc. Notably, the increase in the SOSG fluorescence when $FeSe_2$-ZnPc was subjected to 808 nm light irradiation followed by 640 nm light irradiation (808 nm (+), 640 nm (+)) was much higher than that under the same 640 nm light irradiation conditions without 808 nm light irradiation (808 nm (–) and 640 nm (+)). These results indicated that the release of ZnPc from $FeSe_2$, triggered by 808 nm light, effectively enhanced the photodynamic effect of PSs, thereby increasing the ROS generation capability of $FeSe_2$-ZnPc.

3.4 Strong antimicrobial effect of $FeSe_2$-ZnPc

Inspired by the robust photodynamic/photothermal capability of $FeSe_2$-ZnPc, we evaluated the antimicrobial characteristics of $FeSe_2$-ZnPc. *M. smeg* was chosen as the model bacterium for the antibacterial testing. Briefly, *M. smeg* was incubated with PBS or $FeSe_2$-ZnPc for 6 h, and 808 nm and/or 640 nm laser photoirradiation was subsequently performed. After another 24 h of incubation, the strains were serially diluted 10-fold. The antibacterial results of different groups were determined through a typical colony counting strategy. After

Acta Materia Medica

incubation with $FeSe_2$-ZnPc for 6 h, the number of CFUs was similar to that in the control group (Figure 4a), thereby indicating a negligible effect of $FeSe_2$-ZnPc on *M. smeg*. Subsequently, 808 nm and/or 640 nm photoirradiation was applied. Treatment with PBS followed by light irradiation did not significantly decrease the viability of *M. smeg* (Figure 4b, c), thereby allowing us to exclude the effect of light irradiation on the

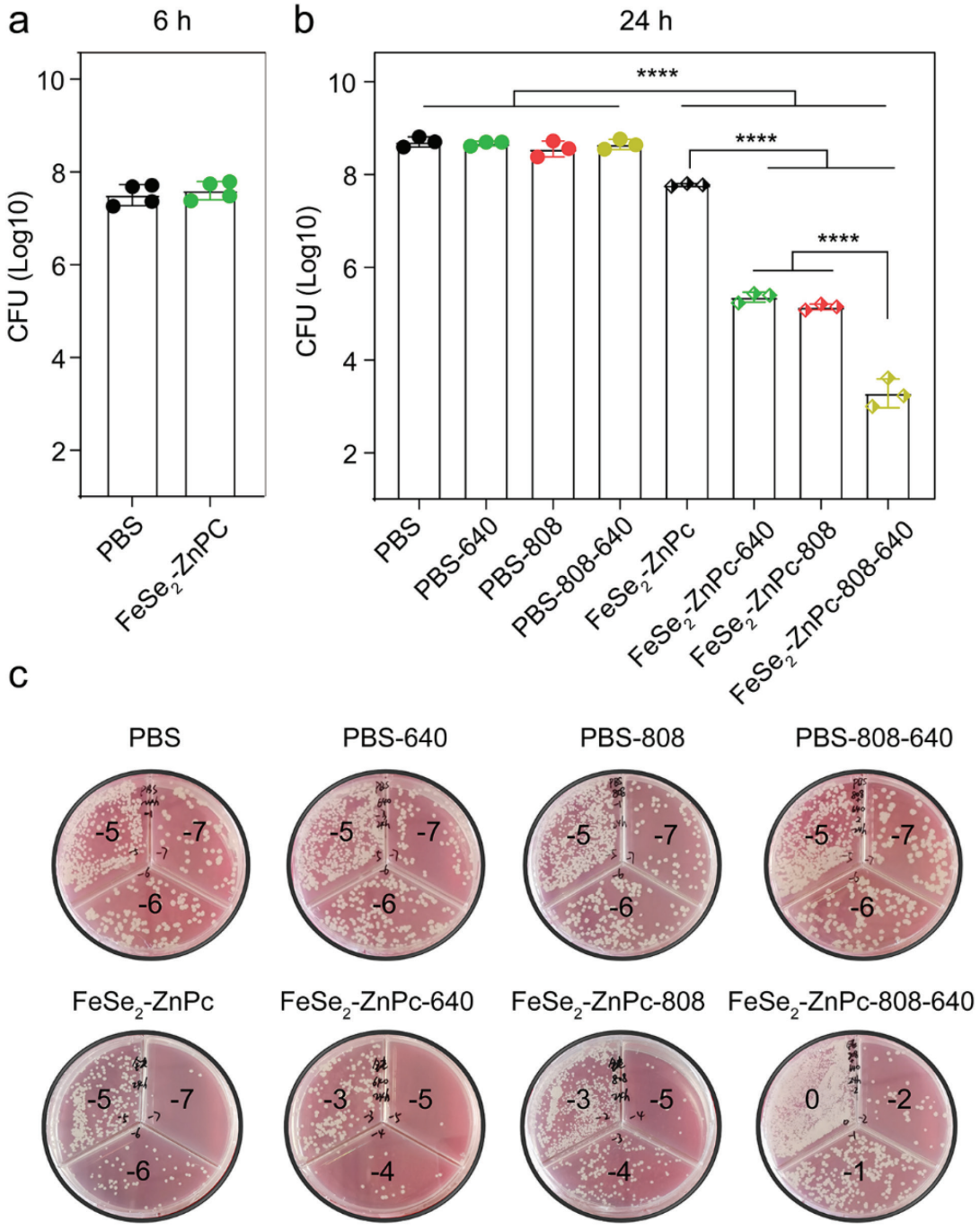

Figure 4 | Antimicrobial effect of $FeSe_2$-ZnPc.
(a) The colony forming units (CFU) of ***M. smeg*** incubated with $FeSe_2$-ZnPc or PBS for 6 h. (b) CFU of ***M. smeg*** detected 24 h after different treatments. All data are presented as the mean ± standard deviation (SD) of three independent replicate experiments. *, $p < 0.05$, **, $p < 0.01$, ***, $p < 0.001$, ****, and $p < 0.0001$. (c) Photographs of ***M. smeg*** colonies after different treatments. The colony plating plot is shown at selected dilutions after 10-fold dilution. The number X on the board (e.g., –7, –6, –5, –4, –3…) indicates that the strains were diluted 10-fold.

CFU of *M. smeg*. The CFU decreased to a greater extent after 24 h treatment with $FeSe_2$-ZnPc than the negative control. Importantly, after irradiation with only an 808 nm or 640 nm laser, moderate inhibition of viability was observed in *M. smeg* treated with $FeSe_2$-ZnPc, thus confirming the potential of $FeSe_2$-ZnPc as a PTT or PDT agent. Notably, the highest cytotoxicity toward mycobacteria was achieved with treatment with $FeSe_2$-ZnPc plus 808 nm and 640 nm light irradiation, thereby confirming that the combination of PTT and PDT increased antimycobacterial potency. Furthermore, no significant differences in the growth of *M. smeg* were observed when equal proportions of PBS and ddH_2O were added to the 7H9 medium (**Figure S4**). The antimicrobial effect of $FeSe_2$-ZnPc was confirmed in *E. coli*, which showed the same results as *M. smeg* (**Figure S5**). The above findings also indicated that the developed $FeSe_2$-ZnP material has a universal bactericidal effect.

4. DISCUSSION

PDT is a promising strategy for the treatment of pathogenic microorganisms. At a specific light irradiation wavelength, PSs transfer photon energy to the surrounding molecular oxygen and consequently generate cytotoxic ROS. Compared with conventional antibiotic therapy, PDT has markedly greater selectivity and fewer adverse effects. ZnPc, a widely used PS, is promising for PDT because of the high quantum yield of ROS and low toxicity. However, the ZnPc inevitably is distributed to normal tissues, particularly the skin, as observed in clinical practice. Under sunlight, ZnPc generates ROS and can subsequently induce skin photosensitivity, thus resulting in unavoidable damage and long-lasting cutaneous photosensitivity. One possible reason for the undesirable phototoxicity is that ZnPc is always in the ON (or active) state, even in normal tissues.

To solve this problem, we report the design and synthesis of a smart PDT system based on a combination of peony-shaped $FeSe_2$ particles and ZnPc PSs. ZnPc PSs are designed to be quenched (OFF state) before administration, because of the proximity between ZnPc and $FeSe_2$. After accumulating in target tissues, ZnPc PSs can be turned on (dequenched) by 808 nm NIR light irradiation, thereby avoiding the potential adverse effects of active PSs. In addition, $FeSe_2$ produces heat under 808 nm NIR irradiation and consequently could be used as a PTT agent. Therefore, our designed liposomes containing ZnPc and $FeSe_2$ may be used as an activatable PDT combined with PTT for the eradication of pathogenic bacteria.

ACKNOWLEDGEMENTS

This work was supported by the National Natural Science Foundation of China (82001946 and 82172279), Beijing Hospitals Authority Innovation Studio of Young Staff Funding Support (202136), and Beijing Municipal Administration of Hospitals Incubating Program (PX2021061).

CONFLICTS OF INTEREST

The authors declare no conflicts of interest.

REFERENCES

[1] Baron VO, Chen M, Hammarstrom B, Hammond RJH, Glynne-Jones P, Gillespie SH, et al.: Real-time Monitoring of Live Mycobacteria with a Microfluidic Acoustic-Raman Platform. *Communications Biology* 2020, 3:236.

[2] Glaziou P, Floyd K, Raviglione MC. Global Epidemiology of Tuberculosis. *Seminars in Respiratory and Critical Care Medicine* 2018, 39:271–285.

[3] Kavunja HW, Biegas KJ, Banahene N, Stewart JA, Piligian BF, Groenevelt JM, et al.: Photoactivatable Glycolipid Probes for Identifying Mycolate-Protein Interactions in Live Mycobacteria. *Journal of the American Chemical Society* 2020, 142:7725–7231.

[4] Sakatos A, Babunovic GH, Chase MR, Dills A, Leszyk J, Rosebrock T, et al.: Posttranslational Modification of a Histone-Like Protein Regulates Phenotypic Resistance to Isoniazid in Mycobacteria. *Science Advances* 2018, 4:eaao1478.

[5] Wakamoto Y, Dhar N, Chait R, Schneider K, Signorino-Gelo F, Leibler S, et al.: Dynamic Persistence of Antibiotic-Stressed Mycobacteria. *Science* 2013, 339:91–95.

[6] Claudi B, Spröte P, Chirkova A, Personnic N, Zankl J, Schürmann N, et al.: Phenotypic Variation of Salmonella in Host Tissues Delays Eradication by Antimicrobial Chemotherapy. *Cell* 2014, 158:722–733.

[7] Aldridge BB, Fernandez-Suarez M, Heller D, Ambravaneswaran V, Irimia D, Toner M, et al.: Asymmetry and Aging of Mycobacterial Cells Lead to Variable Growth and Antibiotic Susceptibility. *Science* 2012, 335:100–104.

[8] Adams Kristin N, Takaki K, Connolly Lynn E, Wiedenhoft H, Winglee K, Humbert O, et al.: Drug Tolerance in Replicating Mycobacteria Mediated by a Macrophage-Induced Efflux Mechanism. *Cell* 2011, 145:39–53.

[9] Liu Y, Busscher HJ, Zhao B, Li Y, Zhang Z, van der Mei HC, et al.: Surface-Adaptive, Antimicrobially Loaded, Micellar Nanocarriers with Enhanced Penetration and Killing Efficiency in Staphylococcal Biofilms. *ACS Nano* 2016, 10:4779–4789.

[10] Zhu X, Zhu Y, Jia K, Abraha BS, Li Y, Peng W, et al.: A Near-Infrared Light-Mediated Antimicrobial Based on Ag/Ti3C2Tx for Effective Synergetic Antibacterial Applications. *Nanoscale* 2020, 12:19129–19141.

[11] Xie X, Sun T, Xue J, Miao Z, Yan X, Fang W, et al.: Ag Nanoparticles Cluster with pH-Triggered Reassembly in Targeting Antimicrobial Applications *Advanced Functional Materials* 2020, 30:2000511.

[12] Majumdar TD, Singh M, Thapa M, Dutta M, Mukherjee A, Ghosh CK. Size-Dependent Antibacterial Activity of Copper Nanoparticles against Xanthomonas oryzae pv. Oryzae-A Synthetic and Mechanistic Approach. *Colloid and Interface Science Communications* 2019, 32:100190.

[13] Ali IH, Ouf A, Elshishiny F, Taskin MB, Song J, Dong M, et al.: Antimicrobial and Wound-Healing Activities of Graphene-Reinforced Electrospun Chitosan/Gelatin Nanofibrous Nanocomposite Scaffolds. *ACS Omega* 2022, 7:1838–1850.

[14] Akhavan O, Ghaderi E. Toxicity of Graphene and Graphene Oxide Nanowalls against bacteria. *ACS Nano* 2010, 4:5731–5736.

[15] Perreault F, De Faria AF, Nejati S, Elimelech M. Antimicrobial Properties of Graphene Oxide Nanosheets: Why Size Matters. *ACS Nano* 2015, 9:7226–7236.
[16] Song J, Kong H, Jang J. Enhanced Antibacterial Performance of Cationic Polymer Modified Silica Nanoparticles. *Chemical Communications* 2009, 36:5418–5420.
[17] Hayden SC, Zhao G, Saha K, Phillips RL, Li X, Miranda OR, et al.: Aggregation and Interaction of Cationic Nanoparticles on Bacterial Surfaces. *Journal of the American Chemical Society* 2012, 134:6920–6923.
[18] Liu S, Wei L, Hao L, Fang N, Chang MW, Xu R, et al.: Sharper and Faster "Nano Darts" Kill More Bacteria: A Study of Antibacterial Activity of Individually Dispersed Pristine Single-Walled Carbon Nanotube. *ACS Nano* 2009, 3:3891–3902.
[19] Qiao Y, Yang C, Coady DJ, Ong ZY, Hedrick JL, Yang YY. Highly Dynamic Biodegradable Micelles Capable of Lysing Gram-Positive and Gram-Negative Bacterial Membrane. *Biomaterials* 2012, 33:1146–1153.
[20] Nguyen TK, Lam SJ, Ho KK, Kumar N, Qiao GG, Egan S, et al.: Rational Design of Single-Chain Polymeric Nanoparticles that Kill Planktonic and Biofilm Bacteria. *ACS Infectious Diseases* 2017, 3:237–248.
[21] Liu L, Xu K, Wang H, Jeremy Tan PK, Fan W, Venkatraman SS, et al.: Self-Assembled Cationic Peptide Nanoparticles as an Efficient Antimicrobial Agent. *Nature Nanotechnology* 2009, 4:457–463.
[22] Lam SJ, Wong EH, Boyer C, Qiao GG. Antimicrobial Polymeric Nanoparticles. *Progress in Polymer Science* 2018, 76:40–64.
[23] Sharma B, Kaur G, Chaudhary GR, Gawali SL, Hassan PA. High Antimicrobial Photodynamic Activity of Photosensitizer Encapsulated Dual-Functional Metallocatanionic Vesicles against Drug-Resistant Bacteria S. aureus. *Biomaterials Science* 2020, 8:2905–2920.
[24] Ravikumar M, Raghav D, Rathinasamy K, Kathiravan A, Mothi EM. DNA Targeting Long-Chain Alkoxy Appended Tin(IV) Porphyrin Scaffolds: Photophysical and Antimicrobial PDT Investigations. *ACS Applied Bio Materials* 2018, 1:1705–1716.
[25] Narayanan N, Kim JH, Santhakumar H, Joseph MM, Karunakaran V, Shamjith S, et al.: Nanotheranostic Probe Built on Methylene Blue Loaded Cucurbituril and Gold Nanorod: Targeted Phototherapy in Combination with SERS Imaging on Breast Cancer Cells. *The Journal of Physical Chemistry. B* 2021, 125:13415–13424.
[26] Klausen M, Ucuncu M, Bradley M. Design of Photosensitizing Agents for Targeted Antimicrobial Photodynamic Therapy. *Molecules* 2020, 25:5239.
[27] Garg P, Kaur G, Sharma B, Chaudhary GR. Fluorescein–Metal Hybrid Surfactant Conjugates as a Smart Material for Antimicrobial Photodynamic Therapy Against Staphylococcus Aureus. *ACS Applied Bio Materials* 2020, 3:4674–4683.
[28] Wang J, You M, Zhu G, Shukoor MI, Chen Z, Zhao Z, et al.: Photosensitizer–Gold Nanorod Composite for Targeted Multimodal Therapy. *Small* 2013, 9:3678–3684.
[29] Wang J, Zhu G, You M, Song E, Shukoor MI, Zhang K, et al.: Assembly of Aptamer Switch Probes and Photosensitizer on Gold Nanorods for Targeted Photothermal and Photodynamic Cancer Therapy. *ACS Nano* 2012, 6:5070–5077.
[30] Cló E, Snyder JW, Voigt NV, Ogilby PR, Gothelf KV. DNA-Programmed Control of Photosensitized Singlet Oxygen Production. *Journal of the American Chemical Society* 2006, 128:4200–4201.
[31] Liu B, Ma R, Zhao J, Zhao Y, Li L. A Smart DNA Nanodevice for ATP-Activatable Bioimaging and Photodynamic Therapy. *Science China Chemistry* 2020, 63:1490.
[32] Lovell JF, Liu TWB, Chen J, Zheng G. Activatable Photosensitizers for Imaging and Therapy. *Chemical Reviews* 2010, 110:2839–2857.
[33] Piao W, Hanaoka K, Fujisawa T, Takeuchi S, Komatsu T, Ueno T, et al.: Development of an Azo-Based Photosensitizer Activated under Mild Hypoxia for Photodynamic Therapy. *Journal of the American Chemical Society* 2017, 139:13713–13719.
[34] Tsuji Y, Yamamoto K, Yamauchi K, Sakai K. Near-Infrared Light-Driven Hydrogen Evolution from Water Using a Polypyridyl Triruthenium Photosensitizer. *Angewandte Chemie International Edition* 2018, 57:208–212.
[35] Jang B, Park JY, Tung CH, Kim IH, Choi Y. Gold Nanorod–Photosensitizer Complex for Near-Infrared Fluorescence Imaging and Photodynamic/Photothermal Therapy In Vivo. *ACS Nano* 2011, 5:1086–1094.
[36] Tian B, Wang C, Zhang S, Feng L, Liu Z. Photothermally Enhanced Photodynamic Therapy Delivered by Nano-Graphene Oxide. *ACS Nano* 2011, 5:7000–7009.
[37] Wang Y, Liu G, Sun L, Xiao J, Zhou J, Yan C. Nd^{3+}-Sensitized Upconversion Nanophosphors: Efficient in Vivo Bioimaging Probes with Minimized Heating Effect. *ACS Nano* 2013, 7:7200–7206.
[38] Liu B, Li C, Yang P, Hou Z, Lin J. 808-nm-Light-Excited Lanthanide-Doped Nanoparticles: Rational Design, Luminescence Control and Theranostic Applications. *Advanced Materials* 2017, 29:1605434.